Available online at www.sciencedirect.com
ScienceDirect
Journal of Catalysis 248 (2007) 258–267
JOURNAL OF CATALYSIS
www.elsevier.com/locate/jcat

Effect of surface area and bulk structure on oxygen storage capacity of $Ce_{0.67}Zr_{0.33}O_2$

Minwei Zhao [a], Meiqing Shen [a,b], Jun Wang [a,*]

[a] *Key Laboratory for Green Chemical Technology of State Education Ministry, School of Chemical Engineering & Technology, Tianjin University, Tianjin 300072, PR China*

[b] *State Key Laboratory of Engines, Tianjin University, Tianjin 300072, PR China*

Received 16 January 2007; revised 6 March 2007; accepted 7 March 2007

Available online 26 April 2007

Abstract

The oxygen storage capacity (OSC) of $Ce_{0.67}Zr_{0.33}O_2$ catalysts were investigated with CO–He pulses at 500 °C and CO–O_2 dynamic pulses at 300–700 °C after redox and hydrothermal treatments. BET, XRD, and EPR were used to study the effects of the pretreatment on the surface and bulk structures of the catalyst. The results show that during the CO–He pulses, migration of oxygen from the bulk to the surface becomes important. The rate of oxygen migration depends on the structure of the solid and the number of the oxygen vacancies in the lattice. The experiments with dynamic pulses of CO–O_2 reveal that DOSC is closely related to the surface area of the samples of the same composition. However, at high temperatures, oxygen in the bulk also contributes to DOSC due to bulk-to-surface migration. A mechanism describing the reaction between the surface oxygen and CO and the oxygen migration process from the bulk to the surface is proposed.
© 2007 Elsevier Inc. All rights reserved.

Keywords: Ceria–zirconia; Oxygen storage capacity; OSC; TWC; CO pulse

1. Introduction

Ceria–zirconia is a key component in three-way catalysts (TWCs) due to its superior thermal stability and oxygen storage capacity (OSC) to pure ceria [1,2]. Its major role is to minimize fluctuation of the air-to-fuel (A/F) ratio at around 14.6 during engine operation, thus ensuring that TWCs work effectively within a narrow operating window near the stoichiometric A/F ratio. Under the transitions between lean and rich operating conditions, OSC stores or releases oxygen, depending on the A/F ratio of the exhaust gas.

It is desirable to focus of the properties of CO oxidation and OSC in one material because CO oxidation is one of the key reactions in the TWC process. In 1984, Yao et al. [3] reported a dynamic method for measuring the total OSC (TOSC) and dynamic OSC (DOSC). Using this method, Descorme et al. [4] and Boaro et al. [5] recently investigated the dynamic OSC behavior of ceria–zirconia with catalyst materials exposed to sequential pulses of CO, He, and O_2. These authors found that the OSC characteristics of Ce–Zr-based materials are affected by material composition, surface area, and the redox reactions occurring on the surface and in the bulk of the materials. Consequently, an important aspect of the OSC behavior of the ceria–zirconia-based materials is the sensitivity of the OSC characteristics to their surface area and bulk structure.

The OSC of ceria–zirconia is intrinsic to its structure [6–12]. A case point is that the redox modification of reduction/oxidation can result in a more homogeneous structure and improve OSC performance. It is believed that significant changes occur in oxide structure, demonstrated as Zr–O coordination variation determined by EXAFS [13]. Fornasiero et al. [14] also attributed the improved oxygen activation by redox treatment to a decreased Zr coordination number. The catalytic activity of ceria–zirconia is independent of surface area [15,16]; on the other hand, oxygen vacancies are found to enhance oxygen mobility. The hopping mechanism of oxygen vacancies relating to structure modification has been proposed to explain the OSC promotion [17]. Likewise, existence of oxy-

* Corresponding author.
E-mail address: wangjun@tju.edu.cn (J. Wang).

0021-9517/$ – see front matter © 2007 Elsevier Inc. All rights reserved.
doi:10.1016/j.jcat.2007.03.005

gen vacancies is also considered as the key factor in OSC stability [18]. In this regard, further insight into the effect of surface and bulk structure on OSC can provide useful information for future ceria–zirconia designs.

The present work investigates the influence of surface area, bulk structure, and pretreatment on the OSC characteristics of ceria–zirconia materials using CO pulse and dynamic pulses of CO and O_2. In addition, reaction mechanism and dynamics are also discussed based on the results.

2. Experimental

2.1. Catalyst preparation

The $Ce_{0.67}Zr_{0.33}O_2$ samples investigated here were prepared by the citric sol–gel method. Citric acid and glycol, as complex reagents, were added to the mixed solution of Ce $(NO_3)_3$ and ZrO $(NO_3)_2$ with the stoichiometric ratio and vigorous stirring. After continuous stirring at room temperature for 2 h, the mixed solution was kept at 80 °C overnight to obtain a wet transparent yellow gel. The gel was dried at 100 °C for 3 h to obtain a sponge-like dry yellow gel, which was then calcined at 300 °C for 30 min and then at 500 °C for 5 h to obtain as-prepared $Ce_{0.67}Zr_{0.33}O_2$ material. The as-prepared sample is designated as the high surface area sample (HA). Samples with moderate surface area (MA) and low surface area (LA) were obtained by treating the HA material under redox conditions. The HA sample was first heated to 800 °C (at a ramp rate of 10 °C/min) under reducing conditions (5% H_2/N_2 flow at 100 mL/min), then held at 800 °C for 0 h (mild reduction) or 10 h (severe reduction). Then these samples were oxidized in air flow (250 mL/min) at 500 °C for 1 h. The resulting oxide samples are designated as the CZ-MA and CZ-LA samples. A sample with severe hydrothermal ageing (SA) was obtained by heating the HA samples to 800 °C (at a ramp rate of 10 °C/min) in a 250-mL/min 10% steam/air atmosphere and keeping them at 800 °C for 5 h. The resulting sample is designated as CZ-SA.

2.2. Characterization

BET surface areas of the samples were measured by N_2 adsorption at 77 K using a Quantachrome NOVA 2000 apparatus. X-ray powder diffraction (XRD) patterns were acquired with an X'Pert Pro diffractometer operating at 40 kV and 40 mA with ferrum-filtered Co$K\alpha$ radiation and a step size of 0.03°. The lattice constants were calculated based on Bragg's law, $2d \sin\theta = k\lambda$, for planes (111), (200), (220), and (311), where d is the distance of crystal plane, θ is the angle of diffraction peak, and λ is the wavelength of Co$K\alpha$ radiation. Crystal sizes were determined using Scherrer's equation calculated based on the (111) plane.

Electron paramagnetic resonance (EPR) spectra at the X band frequency (≈9.7 GHz) were recorded at room temperature with a Bruker A320 spectrometer calibrated with 2,2-diphenyl-1-picrylhydrazyl ($g = 2.0036$). Equal-sized portions of ceria–zirconia samples were placed inside the quartz probe cell. The EPR parameter values were precisely determined from the calculated spectra. The g factor was calculated by the equation $h\upsilon = g\beta H$, where h is Planck's constant, H is the applied magnetic field, and β is Bohr's magneton. The relative concentrations of paramagnetic site intensity were determined as normalized double integrals of EPR spectra using Bruker's WINEPR program.

H_2-TPR experiments were conducted using a Micromeritics AutoChem 2910. The catalyst sample was first purged under N_2 (30 mL/min) at 200 °C for 1 h and then cooled to room temperature. The sample was then exposed to a flow of 5% H_2/Ar (30 mL/min) while the temperature was ramped from room temperature to 900 °C at a rate of 10 °C/min.

2.3. OSC measurement

OSC measurements were obtained using the OSC equipment with a system dead volume of 3.5 mL. A 25-mg catalyst sample diluted with 40 mg of quartz beads was placed at the bottom of heat transfer reactor. The concentrations of the five components (CO, O_2, CO_2, Ar, and He) in the outlet gas were monitored online by a Balzers QMS200 quadrupole spectrometer.

The redox ability of the samples investigated was referred to as the OSC measurement. Two modes were included: CO–He pulse measurements and CO–O_2 pulse measurements. All CO–He pulses for the OSC measurement were applied at 500 °C. A sample was exposed to alternating CO (4% CO/1% Ar/He at 300 mL/min for 5 s) and He (300 mL/min for 20 s) pulses, and the alternating pulsation lasted for 10 CO–He cycles. OSC was calculated by integrating the CO_2 formed, a product between CO and oxygen within the Ce–Zr material, during the pulsation experiment. OSC was expressed as μmol of O per gram of ceria–zirconia catalyst (μmol [O] g^{-1}). TOSC was calculated by summing the OSC of 10 CO pulses.

The dynamic measurements with CO–O_2 pulses were obtained at 300–700 °C at 50 °C intervals. CO (4% CO/1% Ar/He at 300 mL/min for 10 s) and O_2 (2% O_2/1% Ar/He at 300 mL/min for 10 s) streams were pulsed alternately with a pulsation frequency (i.e., the number of CO and O_2 pulses per second) of 0.05 Hz. A pulsation interval of 5 s was used for some experiments (0.1 Hz). A DOSC value was obtained by integrating the CO_2 formed during one CO–O_2 cycle and was expressed as μmol of O per gram of ceria–zirconia catalyst (μmol [O] g^{-1}).

3. Results and discussion

3.1. Surface and structure properties

3.1.1. BET and XRD

The XRD patterns of $Ce_{0.67}Zr_{0.33}O_2$ samples with different surface areas are shown in Fig. 1. The peak profiles show four main peaks between 20° and 80°, indexed as the cubic fluorite ceria–zirconia solid solution. The sharp peaks of aged samples indicate comparable larger crystallites due to the high-temperature treatment. As listed in Table 1, crystallites of four samples are ordered as SA (133 Å) > LA (102 Å) > MA (92 Å) > HA (73 Å). Consistent with our expectations, three

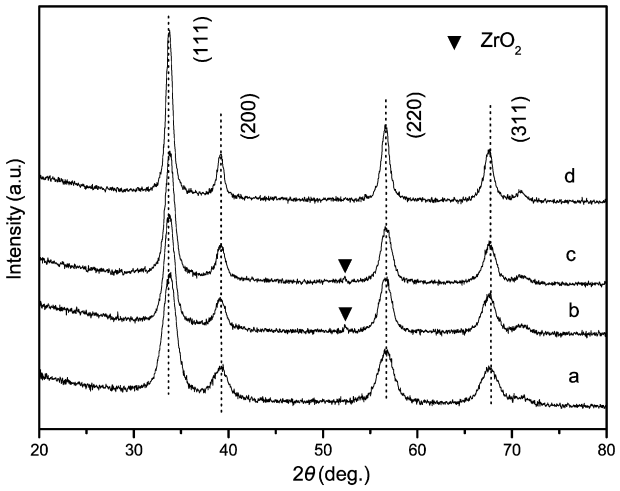

Fig. 1. XRD patterns of $Ce_{0.67}Zr_{0.33}O_2$ samples: (a) HA; (b) MA; (c) LA; (d) SA.

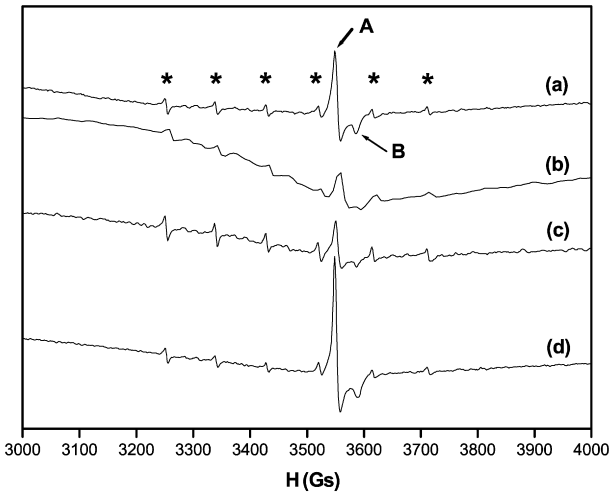

Fig. 2. Characteristics of EPR signals observed at R.T. on $Ce_{0.67}Zr_{0.33}O_2$ samples.

Table 1
S_{BET} and lattice constants and TOSC of $Ce_{0.67}Zr_{0.33}O_2$ samples

Samples	Surface area ($m^2\ g^{-1}$)	Lattice constants[a] (Å)	Crystallite size (Å)	TOSC[b] (μmol g^{-1})
				MV
HA	56	5.3369 (4)	73	1155
MA	22	5.3361 (2)	92	975
LA	14	5.3346 (7)	102	1216
SA	9	5.3416 (3)	133	1223

[a] Lattice constants are calculated by Jade Program, where SD of lattices constants is listed in the corresponding bracket.

[b] TOSC is determined by summarizing OSC of ten CO pulses. Given as mean value, MV; standard deviation, SD. $N = 4$. SD of CO pulse during 1st to 3rd pulses is ranging from ±4 to ±11 μmol g^{-1}. SD of CO pulses during 3rd to 10th is ranging from ±2 to ±4 μmol g^{-1}.

Table 2
Characteristics of EPR signals $Ce_{0.67}Zr_{0.33}O_2$ samples

Samples	EPR parameters		Intensity	Treatment
	A	B		
HA	$g = 1.968$	$g = 1.947$	81	Calcined at 500 °C for 5 h.
MA	$g = 1.962$	$g = 1.943$	4	5% H_2/N_2 for 0 h at 800 °C, reoxidized 500 °C in air for 1 h.
LA	$g = 1.966$	$g = 1.946$	46	5% H_2/N_2 for 10 h at 800 °C, reoxidized 500 °C in air for 1 h.
SA	$g = 1.968$	$g = 1.946$	389	10% steam/air for 5 h at 800 °C.

levels of surface area with the sequence of HA > MA > LA ≈ SA were attained according to the crystallites sintering. Therefore, we initially focused on studying the contribution of surface area to OSC behavior.

With treatment at 800 °C, minor differences in structural properties among the CZ-MA, CZ-LA, and CZ-SA are detected, in addition to the changes in surface area. As shown in Fig. 1, a segregated zirconia phase and decrease in lattice constants are identified on MA and LA samples compared with the HA sample. Calculated by Bragg's law, lattice shrinkage from 5.3369 Å (HA sample) to 5.3361 and 5.3346 Å is observed on MA and LA samples. The shrinkage indicates that, other than Zr separation, separation of larger Ce^{4+} (0.97 Å) ions from the lattice should be taken into consideration for its comparable larger ionic radius, resulting in the lattice constants shrinkage. However, the small crystallites can escape the XRD detection for the peak overlapping [13]. From this aspect, it is a synthetic effect of Zr and Ce separation that results in lattice shrinkage in the MA and LA samples. According to the literature, small isolated diffraction peaks on XRD patterns after redox treatment at 1200 °C are ascribed to the rearrangement of ceria and zirconia cations at redox treatment with the κ-phase ceria–zirconia formation [13]. Our results demonstrate no κ-phase ceria–zirconia, possibly due to comparably low redox temperature; however, due to detection of ZrO_2 species, rearrangements of ceria–zirconia crystal after redox treatment at 800 °C cannot be excluded. Conversely, an opposite tendency of the lattice is observed on the SA sample due to the structural modification induced by calcination in hydrothermal atmosphere, consistent with the previous observation using Raman spectroscopy [10]. In this regard, the structure difference between lattice expansion and shrinkage possibly may be caused by different treatment conditions (i.e., hydrothermal vs redox).

3.1.2. EPR

The EPR spectra of $Ce_{0.67}Zr_{0.33}O_2$ obtained at room temperature are presented in Fig. 2. For all four $Ce_{0.67}Zr_{0.33}O_2$ samples, peaks A and B are observed due to typical characteristic of Ce^{3+} ions containing the unpaired electrons. The features with a six-line hyperfine structure due to Mn^{2+} impurities are marked with asterisks [19]. Peak A ($g = 1.962$–1.968) corresponds to Ce^{3+} in terms of surface structure, and peak B ($g = 1.943$–1.947) is attributed to Ce^{3+} in the bulk [20]. As shown in Table 2, minor differences on g factor among HA, MA, LA, and SA samples may be due to variations in the Ce^{3+} chemical environment. As shown in Table 2, for MA and LA, the g factor shifts to lower value than that of HA, whereas for SA the g factor shifts to a higher value, consistent with the results obtained by XRD after redox and hydrothermal treatments. Therefore, a change in g factor reflects the tendency of lattice distortion.

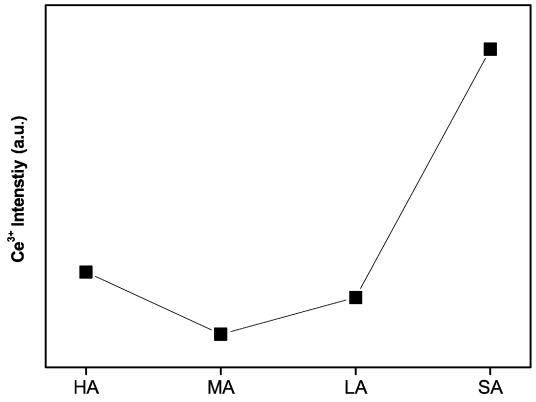

Fig. 3. Integrated Ce^{3+} EPR intensity of $Ce_{0.67}Zr_{0.33}O_2$ samples.

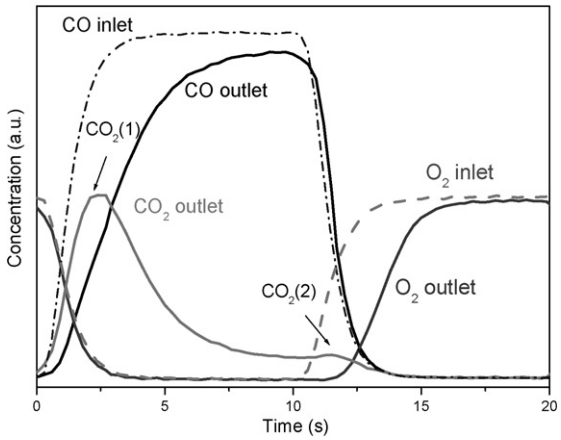

Fig. 4. Representative transition curve with alternate dynamic pulses of 4% CO/1% Ar/He (10 s) and 2% O_2/1% Ar/He (10 s) under 0.05 Hz. (Full line: gas of outlet; dotted line: gas of inlet.)

In addition, Ce^{3+} intensity per gram sample is obtained by normalized double integrals of EPR spectra using Bruker's WINEPR program. As shown in Fig. 3, the MA and LA samples have a lower Ce^{3+} concentration than the HA sample, whereas the SA sample has a higher Ce^{3+} concentration than the HA sample. The Ce^{3+} intensity in the EPR spectra exhibits a controversial tendency between redox and hydrothermal treatment. Both the EPR and XRD results suggest that redox and hydrothermal treatments induce an opposite effect on Ce^{3+} intensity similar to lattice variation. Furthermore, LA exhibits higher Ce^{3+} concentration than MA, indicating the longer reduced H_2 treatment is more favorable for Ce^{3+} creation. Likewise, structure modification on ceria–zirconia under redox treatment is also found to be related to mild oxidation and severe oxidation treatments, where mild oxidation is more favorable for pyrochlore-related structure associated with oxygen vacancies [18]. Here no signal of oxygen vacancies is detected, and it is thought that low relaxation spin time at room temperature makes the detection of oxygen vacancies like O_2^- and O^- impossible. However, the signals of Ce^{3+} and Zr^{3+} are intrinsic to the corresponding oxygen vacancies, such as O_2^-–Ce^{4+} and O_2^-–Zr^{4+}, which is the electron transfer between O_2^- and cation [21]. Therefore, the number of Ce^{3+} obtained from integrating the EPR spectra can reveal the real concentration of oxygen vacancies with the sequence of SA > HA > LA > MA (see Fig. 3). In conclusion, hydrothermal treatment favors the formation of the oxygen vacancies more than redox treatment does.

3.2. OSC performance

3.2.1. Dynamic OSC with alternate dynamic pulses of CO and O_2

The representative evolution curves of CO, O_2, and CO_2 during the process of alternate dynamic pulse of 4% CO/1% Ar/He and 2% O_2/1% Ar/He under 0.05 Hz are shown in Fig. 4, where only one CO–O_2 cycle is selected from the continuous transient CO–O_2 pulses to represent the dynamic OSC curve. The solid line denotes outlet gas concentration, and the dotted line denotes inlet gas concentration. Back-mixing in reactor is minimized by decreasing the reactor's dead volume. The behavior of doublet CO_2 peaks under CO–O_2 pulses is in a good agreement with the results published in the literature [4,5,22,23]. The CO_2 peak appears at the start of the CO pulse is designated as the first CO_2 peak, designated CO_2 (1), and the second peak of CO_2, designated CO_2 (2), occurs during the transition from CO pulse to O_2 pulse.

Fig. 5 reports the DOSC amounts of HA, MA, LA, and SA samples from alternate dynamic pulses of CO and O_2 with 0.05 or 0.1 Hz, where DOSC amount is calculated by integrating the CO_2 formed with one CO–O_2 cycle. First, DOSC increases with increasing temperature, which may be due to the more activated oxygen and accelerated oxygen back-spillover process. Second, DOSC decreases with increasing pulsing frequency; however, DOSC tendency among four Ce–Zr samples is consistent under 0.05 and 0.1 Hz. Higher pulsing frequencies decrease the residence time for CO; thus, less bulk oxygen has insufficient time to migrate to the surface for CO oxidation, resulting in decreased CO_2 production.

Surface specific area greatly affects DOSC behavior. The span of temperature sensitivity of DOSC may be divided into three parts: 300 °C or below, 350–550 °C, and >550 °C. At $T \leqslant 300$ °C, DOSC is not sensitive to the surface structure of ceria–zirconia because the surface oxygen is not activated (confirmed by the TPR results presented in Section 3.2.2). Between 350 and 550 °C, DOSC follows the ranking HA > LA > MA > SA, which is the same as the ranking of their surface area except LA. When the temperature is increased to above 550 °C, the DOSC ranking becomes HA > SA > LA > MA. The DOSC of all samples except MA are almost the same at 700 °C. We can conclude that surface contribution to OSC is more important under dynamic OSC measurements. However, the surface contribution to dynamic OSC is dependent on temperature, and this contribution is more important in the low-temperature range (350–550 °C). On the other hand, the surface effect on dynamic OSC decreases with increasing temperature, as demonstrated by the DOSC of the four samples crossing at one point at 700 °C with a loop formation. TPR results (see Section 3.2.2) show that at 700 °C, almost all of the surface and bulk oxygen participates in H_2 reduction. Due to increased bulk oxygen activation at high temperature, surface oxygen decreases sharply

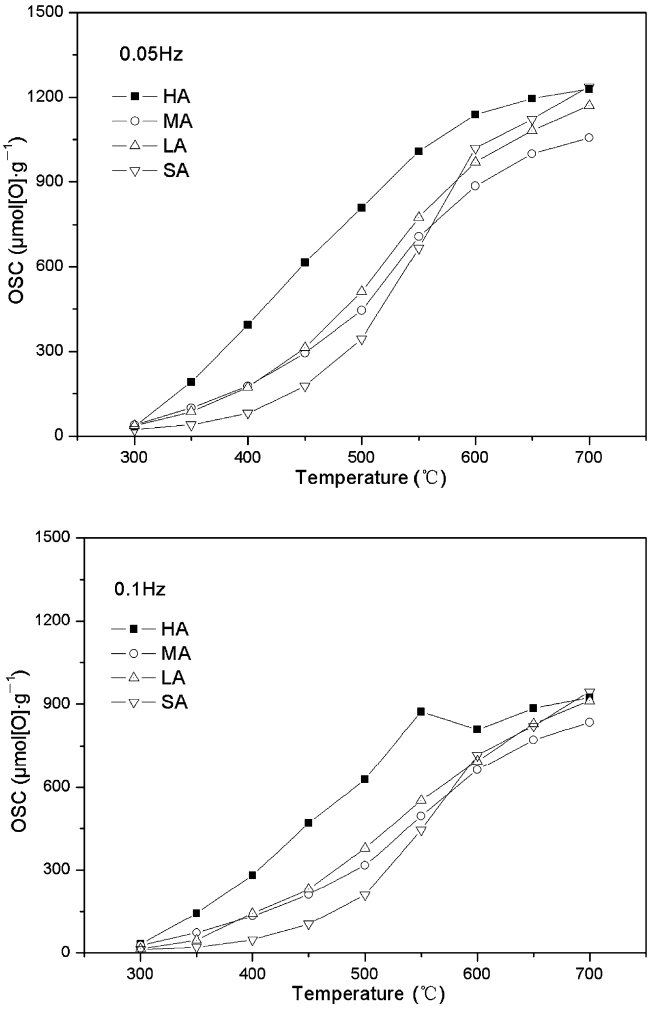

Fig. 5. DOSC of $Ce_{0.67}Zr_{0.33}O_2$ samples with alternate dynamic pulses of 4% CO/1% Ar/He and 2% O_2/1% Ar/He under 0.05 and 0.1 Hz.

to a comparably lower proportion in DOSC. To some extent, the behavior of DOSC at high temperature (i.e., 700 °C) is similar to the behavior of TOSC (see Section 3.2.2). For sample MA, the comparably low TOSC amount is due to the lower lattice distortion intrinsic to the bulk structure. Consistent with the DOSC behavior of MA at 700 °C, the bulk structure plays a more important role in DOSC at high temperature.

The abnormity between the MA and LA samples independent of surface area suggests that other than quantity of surface area, the structure of LA (10 h in H_2), which underwent a longer H_2 reduced treatment, is more favorable for OSC promotion than that of MA (0 h in H_2), even though LA has a smaller surface area. As per the XRD and EPR results, the LA sample has greater lattice distortion than MA sample, ascribed to the longer reduced treatment. This indicates that the LA sample behaves more similarly to the pyrochlore-type structure than the MA sample; accordingly, the pyrochlore-type structure is a key factor in determining the redox response [18]. More precisely, the promotion of reduction on ceria–zirconia is associated with the extent of cation ordering with redox treatment, even if the partial ordering at the surface can promote the reduction behavior [24,25]. This theory is also supported by the effect of repeated redox treatment, which promotes the OSC performance of ceria–zirconia due to lattice distortion under reduced atmosphere [7]. More importantly, it has been reported that cation ordering is associated with the change of entropy of reduction, resulting in changes in reduction behavior [26]. Consistent with the results of Conesa, different arrangements with different energies, which are influenced by the preparation or subsequent treatments, may affect the reducibility behavior [27]. Therefore, the abnormity between MA and LA samples is derived from structure modification, whereas lattice distortion contributes to the higher oxygen mobility.

To quantify analysis of the rates of oxygen release, the first peak CO_2 (1) of DOSC (i.e., the initial CO_2 produced curve ranging in 2 s, which is more effective under high frequency A/F fluctuation) was investigated, with CO_2 (1) measured as a function of surface area. Fig. 6 shows the CO_2 evolution curves during alternating CO and O_2 pulses at three temperatures, 450, 550, and 650 °C. The corresponding DOSC amounts shown in Fig. 5 are calculated by integrating the peak area under the CO_2 curve during one CO–O_2 cycle. At 450 and 550 °C, the slopes of CO_2 (1) from the start are proportional to the CO oxidation rate of these samples and follow the order HA > MA > LA > SA, the same as for BET surface areas. However, the slopes of CO_2 (1) of these samples at 650 °C are about the same. This suggests that at high temperature, surface area no longer controls the oxidation rate, which is consistent with the DOSC results shown in Fig. 5.

As suggested by Hori et al. [16], the CO_2 production rates at the slope are calculated as

$$\frac{\int_{t_0}^{t_1} CO_2\ \text{Signal}}{t_1 - t_0} = \text{Rate}\ [\mu\text{mol of}\ CO_2/\text{s}], \tag{1}$$

where t_1 is the time when the stoichiometry of the catalyst reaches $Ce_{0.67}Zr_{0.33}O_{1.998}$, and t_0 is the starting time for the CO pulse, which is always equal to 0 s in our study. $\int_{t_0}^{t_1} CO_2$ Signal is the integrated peak area from t_1 to t_0, and Rate [μmol of CO_2 g^{-1} s^{-1}] is the initial CO_2 production rate ranging from t_1 to t_0.

As shown in Table 3, the CO_2 production rates for HA, MA, LA, and SA at 450 and 550 °C occur in the order HA (19.2 μmol g^{-1} s^{-1}) > MA (14.8 μmol g^{-1} s^{-1}) > LA (10.7 μmol g^{-1} s^{-1}) > SA (7.5 μmol g^{-1} s^{-1}), the same as the order of their surface areas. At 650 °C, the CO_2 production rates of HA (21.1 μmol g^{-1} s^{-1}), MA (22.9 μmol g^{-1} s^{-1}), LA (19.0 μmol g^{-1} s^{-1}), and SA (21.3 μmol g^{-1} s^{-1}) are about the same, regardless of surface area. This should be due to the different rate-determining steps at these temperatures. According to the literature [28], the E–R pathway for CO oxidation is more likely when the CO pulse switches to the catalyst with less adsorbed CO on the surface.

Assuming that the experiment follows the E–R pathway, according to Hori et al. [16], the concentrations of surface oxygen are estimated as 221 μmol g^{-1} on HA, 84 μmol g^{-1} on MA, 54 μmol g^{-1} on LA, and 36 μmol g^{-1} on SA. (The surface oxygen is equal to the 1/4 of total number of surface oxygen multiplied by X, where X is the $Ce_xZr_{1-x}O_2$ [16].) Clearly, at low temperatures, the CO oxidation rate is determined by

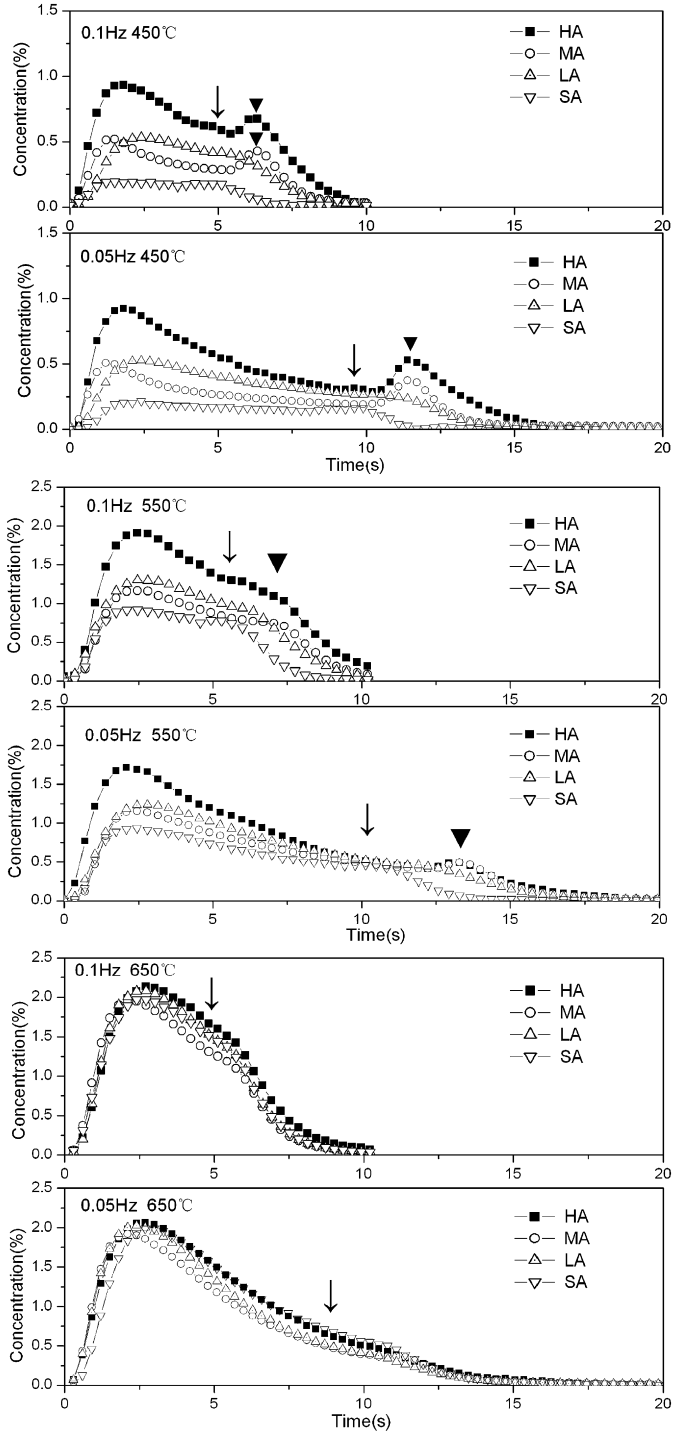

Fig. 6. CO_2 response peaks with alternate dynamic pulses of 4% CO/1% Ar/He and 2% O_2/1% Ar/He under 0.05 and 0.1 Hz.

the amount of surface oxygen [O_s] available (step 2, Table 4). However, at high temperatures (650–700 °C), rapid bulk oxygen migration to the surface is important for CO oxidation, as supported by the similar starting slopes of the CO_2 curves regardless of surface area. Because of low adsorption of CO on the ceria surface and the elevated temperatures at which we operate, the E–R mechanism is thought to be predominant here. Thus, oxygen back-spillover to the surface should be rapid [28].

Table 3
CO_2 production rate of $Ce_{0.67}Zr_{0.33}O_2$ samples under 0.1 Hz

Samples	Rate of CO_2 production (μmol g^{-1} s^{-1})[a]					
	450 °C	$t_1 - t_0$	550 °C	$t_1 - t_0$	650 °C	$t_1 - t_0$
HA	19.2	0.67–0 s	20.1	0.67–0 s	21.1	0.67–0 s
MA	14.8	0.87–0 s	17.8	0.81–0 s	22.9	0.56–0 s
LA	10.7	1.20–0 s	15.6	0.82–0 s	19.0	0.68–0 s
SA	7.5	1.35–0 s	12.7	1.01–0 s	21.3	0.60–0 s

[a] Rate of CO_2 production refers to as the rate at t_0 when CO pulse into the catalysts. Time range from t_1 to t_0 refers to as the calculated rate of CO_2 production.

Fig. 7 shows the relationship between the rates of CO_2 (1) and $1/T$ (10^3) based on the calculated CO_2 production rates. The slopes of the lines are related to the apparent activation energy, which are ordered as HA < MA < LA < SA. This ranking is inversely proportional to the crystallite size. According to the literature, larger crystallites are more difficult to be reduced than smaller ones, as has been confirmed by computer simulations calculating the energy demand of taking oxygen ions from the surface of crystal cluster [29]. It is shown that the energy required to reduce the cluster generally increases with increasing cluster size. Therefore, materials with larger surface areas and smaller crystallite sizes are more favorable for oxidizing CO at lower temperatures. It is also noted that CO_2 production rates released from CO_2 (1) (Fig. 6) at 450 and 550 °C and followed the same order, HA > MA > LA > SA, as that of the DOSC results in Fig. 7.

A mechanism for CO_2 (1) at the start of the CO pulse may be proposed involving surface reactions between CO and surface oxygen sites when the solid surface is in a full-oxidation state (step 2, Table 4). Here the CO catalytic oxidation is noteworthy, because the overlap between CO and O_2 pulses may be a source of CO_2 formation. Descorme et al. [4] reported that at a 1-Hz frequency of CO–O_2 measurement, CO catalytic oxidation occurs due to the coexistence of gas-phase CO and O_2 on a partially oxidized solid surface [4]. The catalytic reaction between CO and O_2 must be a surface reaction on solid ceria–zirconia. One prerequisite for CO catalytic oxidation is that CO and O_2 are coadsorbed on the surface with consumption of reactants. It is essential that, at a CO–O_2 frequency of 1 Hz, CO consumption and O_2 consumption occur simultaneously in the overlap range. In Fig. 4, at low frequency (0.1 and 0.05 Hz) at the start of CO, curve overlapping between $O_{2\ \text{outlet}}$ and $O_{2\ \text{inlet}}$ suggests no gas oxygen consumption during the overlap. Therefore, the effect of CO catalytic oxidation can be avoided at the present low-frequency CO–O_2 measurement due to separation of CO consumption and O_2 consumption at the overlap.

After surface oxygen reduction, when the solid surface is in a slightly reduced state, surface reaction between the adsorbed CO and the oxygen that has migrated from the bulk (step 4, Table 4) will affect the CO oxidation. An L–H-type reaction cannot be ignored for strong CO adsorption at Ce^{3+} sites on reduced ceria–zirconia [30]. The IR results during a CO pulse experiment obtained by Holmgren also confirm that reduced Ce^{3+} sites favor CO adsorption [31,32], and peaks on CO_2 (1) (designated with arrows) further suggest that CO_2 production

Table 4
Proposed mechanisms for doublet CO_2 peaks during a single dynamic CO–O_2 cycle

Step number	CO pulse process	Kinetic expression
1	$CO(g) + * \Leftrightarrow CO*$	$r_1 = K_{1a}[CO](1-\theta_{CO*}) - K_{1a}(\theta_{CO*})$
2	$CO* + O_s \rightarrow CO_2* + \square$	$r_2 = K_2[CO*][O_s]$
3	$O_b + \square \rightarrow O_s*$	$r_3 = K_3([O_b] - [O_s*])/L$ [16]
4	$CO* + O_s* \rightarrow CO_2*$	$r_4 = K_4[CO*][O_s*]$
5	$CO_2* \Leftrightarrow CO_2(g) + *$	$r_5 = K_{5a}(\theta_{CO_2*}) - K_{5a}[CO_2](1-\theta_{CO_2*})$
	O_2 pulse process	
6	$CO_2* \rightarrow CO_2(g) + *$	$r_6 = K_6[CO_2*]$
7	$O_2(g) + \square \rightarrow 2O_s*$	$r_7 = K_7[O_2][\square]$
8	$O_s* + \square \rightarrow O_b + *$	$r_8 = K_8([O_s*] - [O_b])/L$ [16]
9	$O* + CO* \rightarrow CO_2(g) + 2*$	$r_9 = K_9[CO*][O*]$

Note. ∗: active site; (g): gas phase; □: oxygen vacancies; b: bulk oxygen sites; s: surface oxygen site; L: characteristic length of the diffusion.

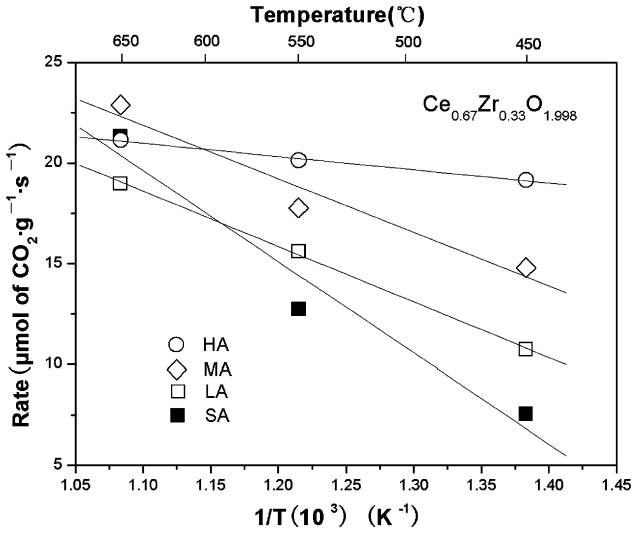

Fig. 7. Arrhenius plot for different surface area $Ce_{0.67}Zr_{0.33}O_2$ samples.

is affected by the bulk O_2 diffusion when surface oxygen is consumed. A clear effect of surface area on the CO_2 (1) peak indicates the importance of the concentration of surface oxygen sites for CO oxidation, as demonstrated in the CO_2 concentration of the four samples, ordered as HA > LA > MA > SA. Noteworthy is the abnormity of CO_2 concentrations between MA and LA samples, which is consistent with the DOSC results shown in Fig. 5. On the other hand, CO oxidation at this stage determines the corresponding order of DOSC in the four samples. Lower surface oxygen sites of the LA sample relative to the MA sample indicates that other than surface oxygen sites, migrated bulk oxygen [O_b] (step 3, Table 4) in the LA structure obviously also affects CO_2 production. The greater distorted and pyrochlore-related structures in the LA sample should be responsible for the higher oxygen mobility. Meanwhile, the CO_2 curve at 650 °C shows that the CO_2 difference by surface area decreases with increasing temperature, suggesting the importance of [O_s∗] (step 4, Table 4) to DOSC, and they may have comparable oxygen mobility near the surface region at high temperatures. Consequently, after surface oxygen reductions during initial 2 s, a synthetic effect of surface oxygen sites [O_s] and migrated oxygen [O_b], determines the CO_2 production of step 4. It is confirmed that at high temperature, bulk oxygen related to structure determines the DOSC performance, consistent with the DOSC results shown in Fig. 5. Furthermore, CO oxidation during CO–O_2 measurement occurs mostly on the surface region due to the high frequency of gas alternation, whereas for TPR measurement, the bulk structure is important, because oxygen mobility is closely related to bulk structure.

The second CO_2 peak of the CO–O_2 pulsation experiment, CO_2 (2), is marked by a solid triangle in Fig. 6. Increasing surface area increases CO_2 (2). CO and CO_2 possibly can be adsorbed simultaneously on the surface when switching from CO to O_2. Boaro et al. [5] considered that CO_2 (2) is formed following a two-step sequence: CO is first adsorbed on the Ce^{3+} sites, forming carbonate–bicarbonate, which is then desorbed as CO_2 on switching the gas stream from CO to O_2. The peak intensity of CO_2 (2) is proportional to the amount of CO_2 adsorbed on surface Ce^{3+} sites. The formation of CO_2 (2) is also reported as a result of the reaction between O_2 and the adsorbed CO via the L–H reaction mechanism [30]. At low temperatures, oxygen adsorption should be the rate-limiting step, because the adsorption of O_2 is weaker than that of CO. Therefore, the active surface area plays an important role in CO_2 (2) formation at low temperatures. At high temperatures (e.g., 650 °C), O_2 adsorption increases, however, resulting in similar CO_2 (2) evolution for all materials. The disappearance of CO_2 (2) occurs in the order SA < LA < MA < HA. Higher surface coverage of both CO_2 and CO is thought to favor the formation of CO_2 (2) [22]. In this regard, surface area plays an important role in affecting the CO_2 production curve and thus DOSC performance.

Based on our experimental results, we can propose possible mechanisms for the dynamic pulsation of CO and O_2 (Table 4). A potential process for oxygen migration and transfer during CO–O_2 dynamic pulses is schematically shown in Fig. 8.

3.2.2. *Total OSC with CO–He pulses and H_2-TPR*

To study the total oxygen available under anaerobic atmosphere, CO pulse with He interval was used to observe the oxygen migration behavior in intrinsic ceria–zirconia. Fig. 9 depicts the representative OSC measurements with 4%

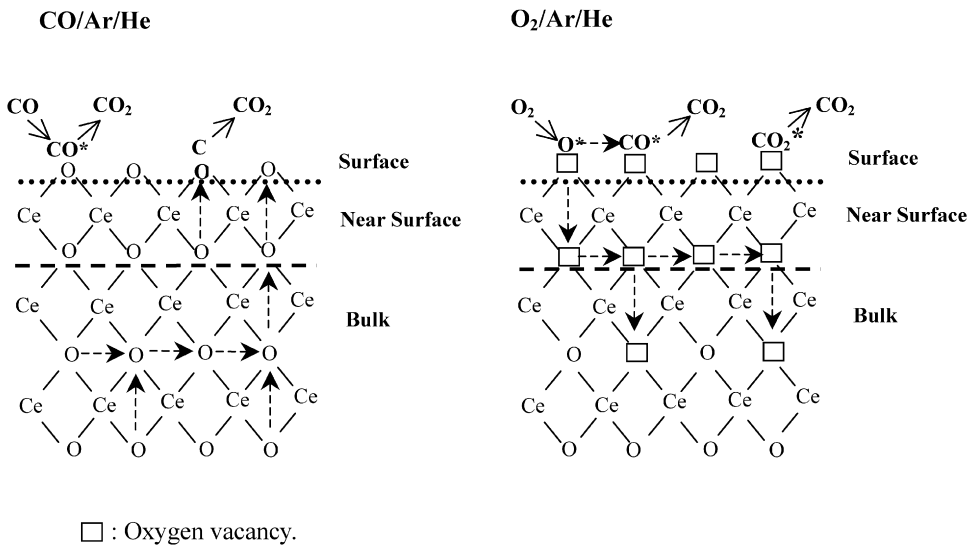

Fig. 8. Reaction mechanism and oxygen migration process with alternate dynamic pulses of CO–O_2.

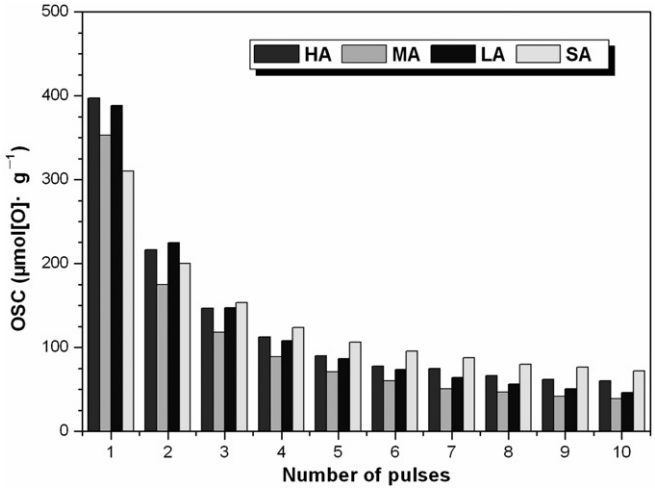

Fig. 9. OSC performance of $Ce_{0.67}Zr_{0.33}O_2$ samples with alternate pulses of 4% CO/1% Ar/He and pure He at 500 °C.

CO/1% Ar/He pulses at 500 °C in ten repeated CO (5 s)–He (20 s) cycles. The amount of available OSC decreases with increasing pulse number. The amount of OSC during each CO pulse is obtained by integrating peak area under the CO_2 curve, whereas the available TOSC is calculated by summing the OSCs of ten CO pulses. As shown in Table 1, the TOSCs of four samples are very close, with order SA (1223 μmol g^{-1}) ≈ LA (1216 μmol g^{-1}) ≈ HA (1155 μmol g^{-1}) > MA (975 μmol g^{-1}), which is independent of the value of specific surface area [33].

Fig. 9 shows that from the third to tenth CO pulses, OSC during each CO pulse follows the order SA > HA > LA > MA. Interestingly, this order is consistent with the Ce^{3+} concentration determined by EPR measurement. In present study, the order of CO (5 s)–He (20 s)–CO (5 s) measurement is interpreted as a process of oxygen migration by pulse number. He purge intervals make the oxygen migration from bulk to the surface. From this aspect, the corresponding number of CO pulse in Fig. 9 represents the timed-resolved OSC under anaerobic atmosphere. At initial CO pulses, CO oxidation occurs almost with the oxygen from the surface and near-surface regions. With the surface and near-surface oxygen reduction, latter CO pulses are almost oxidized by bulk oxygen in a two-step process, involving absorption of CO on the surface of the support and reaction with the oxygen from bulk. Bulk oxygen migration is the rate-determinating step, which can be seen as a function of the intrinsic structure of the material and a rate-determining step for the overall redox process [8]. A direct relationship between lattice defects and OSC was detected by Mamontov et al., suggesting that oxygen defects are the sources of OSC in ceria-based material [34]. Moreover, intrinsic microstructure variation of ceria–zirconia on the Zr coordination could be correlated to oxygen mobility [14,35]. This is the primary reason why ceria–zirconia materials are being used in TWC in place of pure ceria. Therefore, the bulk structures modified by hydrothermal and redox treatments have different influences on the oxygen migration rate from the bulk to the surface on CO pulses.

Defects play another role in the oxygen storage process when precious metal is supported on ceria–zirconia, which is the usual application in practice. This affect of precious metal on oxygen defects is widely recognized [36,37]. Oxidation of Pt in Pt/ceria–zirconia catalyst reflects electron transfer from metal to ceria–zirconia, indicating slightly reduced Ce associated with oxygen vacancy formation [36]. This effect was also supported by the finding that Pt, Rh, and Pd supports promote the reducibility of surface ceria–zirconia [9]. Due to the higher potential of the Ce^{4+}/Ce^{3+} couple (1.61 eV) compared with the Pt^{2+}/Pt^0, Rh^{3+}/Rh^0, and Pd^{2+}/Pd^0 couples, oxygen vacancies play important roles of carriers to determine the oxygen spillover and back-spillover processes at precious metal/ceria–zirconia interfaces [37]. In this regard, oxygen vacancy is the determining factor in bulk oxygen mobility. The synthetic effect between precious metal and defect structure merits further investigation.

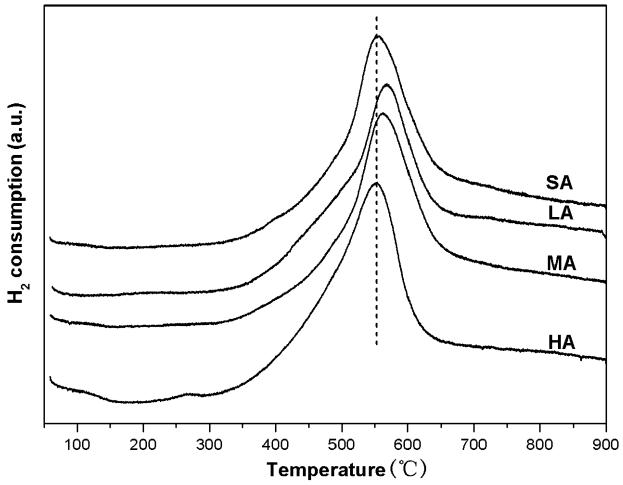

Fig. 10. H_2-TPR profiles of $Ce_{0.67}Zr_{0.33}O_2$ samples.

To confirm the consistency of the TOSC results under CO pulses, TPR for the fresh and aged HA samples, as well as MA, LA, and SA samples, were carried out. The TPR profiles are shown in Fig. 10. In agreement with the DOSC measurements, oxygen reduction starts from ca. 300 °C, suggesting that almost no oxygen is activated to oxidation below 300 °C. The HA sample shows a single H_2 reduction peak at 554 °C. The H_2 consumption is a result of reduction of bulk oxygen, which is usually observed on zirconia-doped ceria samples. Similar H_2 reduction peaks are observed on the MA (564 °C), LA (568 °C), and SA (552 °C) samples, in agreement with the TPR results of Vidal et al. [8], which are less dependent on surface area. It seems that oxygen migration occurs at lower temperatures on hydrothermally treated samples than on the redox-treated samples. The total H_2 consumption is constant even after a reduction treatment at 800 °C, consistent with the CO–He pulse results. The H_2 consumption has no correlation with specific surface area because TPR probes the bulk structure.

Accordingly, the SA sample has the highest concentration of Ce^{3+} on the EPR spectra and the fastest oxygen migration rate during CO oxidation. A correlation is found between the concentration of Ce^{3+} and oxygen migration rate for all samples, and the concentration of Ce^{3+} and the migration rate follow the order SA > HA ≈ LA > MA. The concentration of Ce^{3+} becomes more significant after aging, as shown in the TPR pulse results. Higher OSC is consistent with the high oxygen vacancy mobility deduced from electroconductivity measurements on ceria–zirconia materials [38]. Thus, we can conclude that diffusion of oxygen vacancies related to oxygen migration is critical to OSC performance. Previous reports have shown that the traditional hopping mechanism illustrates the oxygen migration process by interstitial oxygen vacancies, which are closely correlated to OSC by TPR [17]. The migration rate of the bulk oxygen to the surface depends mainly on the bulk structure of the solid, especially on the number of the oxygen vacancies. The decreased number of oxygen available by the increasing pulse number, as shown in Fig. 9, suggests that the gradually decreasing migration of oxygen from the bulk to the surface may be attributed to the lengthened migration pathway due to consumption of surface oxygen ions in the anaerobic atmosphere.

4. Conclusion

We have investigated the OSC of $Ce_{0.67}Zr_{0.33}O_2$ with three levels of surface area by means of anaerobic CO–He pulse and dynamic CO–O_2 measurements. CO–He pulsation experiments revealed that the amount of oxygen available for CO oxidation is intrinsic to the structure and is independent of the surface area. EPR showed that the oxygen migration rate from bulk to surface is related to the structural vacancies of the material, and these vacancies are favored by mild hydrothermal treatment to a redox treatment.

Our dynamic experiments with CO–O_2 pulses showed a strong dependence of OSC on surface area, which decreased at higher temperatures. Oxygen migration at high temperatures is considered as the rate-determining step for CO oxidation. The rate of oxygen release or CO_2 formation is related to the amount of surface oxygen and the crystallite size of ceria–zirconia. A kinetic scheme has been proposed to explain the feature of CO_2 doublet; this proposed mechanism can explain the pathways of CO–O_2 pulses in detail.

Acknowledgments

Financial support was provided by the National Basic Research Program (also called the 973 Program) of China (grant 2004CB719503) and by the Program for Introducing Talents of Discipline to Universities of China (grant B06006). The authors also are grateful for the support of the Program of New Century Excellent Talents in University (grant NCET-06-0243).

References

[1] J. Kašpar, P. Fornasiero, N. Hickey, Catal. Today 77 (2003) 419.
[2] J. Kašpar, P. Fornasiero, J. Solid State Chem. 171 (2003) 19.
[3] H.C. Yao, Y.F.Yu. Yao, J. Catal. 86 (1984) 254.
[4] C. Descorme, R. Taha, N.M. Moral, Appl. Catal. A Gen. 223 (2002) 287.
[5] M. Boaro, F. Giordano, S. Recchia, Appl. Catal. B Environ. 52 (2004) 225.
[6] J. Kašpar, P. Fornasiero, M. Graziani, Catal. Today 50 (1999) 285.
[7] H. Vidal, J. Kašpar, M. Pijolat, Appl. Catal. B Environ. 27 (2000) 49.
[8] H. Vidal, J. Kašpar, M. Pijolat, Appl. Catal. B Environ. 30 (2001) 75.
[9] P. Fornasiero, R. Di Monte, G. Ranga Rao, J. Catal. 151 (1995) 168.
[10] J. Kašpar, P. Fornasiero, G. Balducci, Inorg. Chim. Acta 349 (2003) 217.
[11] F. Esch, S. Fabris, L. Zhou, Science 309 (2005) 752.
[12] F. Dong, A. Suda, T. Tanabe, Catal. Today 93–95 (2004) 827.
[13] Y. Nagai, T. Yamamoto, T. Tanaka, Catal. Today 74 (2002) 225.
[14] P. Fornasiero, E. Fonda, R. Di Monte, J. Catal. 187 (1999) 177.
[15] M. Boaro, C.D. Leitenburg, G. Dolcetti, J. Catal. 193 (2000) 338.
[16] C.E. Hori, A. Brenner, K.Y. Simon Ng, Catal. Today 50 (1999) 299.
[17] P. Fornasiero, J. Kašpar, M. Graziani, Appl. Catal. B Environ. 22 (1999) L11.
[18] M.P. Yeste, J.C. Hernández, S. Bernal, Chem. Mater. 18 (2006) 2750.
[19] A. Martínez-Arias, M. Fernández-García, L.N. Salamanca, J. Phys. Chem. B 104 (2000) 4038.
[20] J.B. Wang, Y.L. Tai, W.P. Dow, Appl. Catal. A Gen. 218 (2001) 69.
[21] A. Martínez-Arias, M. Fernández-García, C. Belver, Catal. Lett. 65 (2000) 197.
[22] S. Hilaire, X. Wang, T. Luo, Appl. Catal. A Gen. 215 (2001) 271.

[23] N. Hickey, P. Fornasiero, J. Kašpar, J. Catal. 200 (2001) 181.
[24] I. Alessandri, M.A. Bañares, L.E. Depero, Top. Catal. 41 (2006) 35.
[25] T. Montini, N. Hickey, P. Fornasiero, Chem. Mater. 17 (2005) 1157.
[26] P.R. Shah, T. Kim, G. Zhou, Chem. Mater. 18 (2006) 5363.
[27] J.C. Conesa, J. Phys. Chem. B 107 (2003) 8840.
[28] R.H. Nibbelke, A.J.L. Nievergeld, J.H.B.J. Hoebink, Appl. Catal. B Environ. 19 (1998) 245.
[29] H. Cordatos, D. Ford, R.J. Gorte, J. Phys. Chem. 100 (1996) 18128.
[30] C.N. Costa, S.Y. Christou, G. Georgiou, J. Catal. 219 (2003) 259.
[31] E.S. Putna, R.J. Gorte, J.M. Vohs, J. Catal. 178 (1998) 598.
[32] A. Holmgren, B. Andersson, D. Duprez, Appl. Catal. B Environ. 22 (1999) 215.
[33] E. Aneggi, J. Llorca, M. Boaro, J. Catal. 234 (2005) 88.
[34] E. Mamontov, T. Egami, R. Brezny, J. Phys. Chem. B 104 (2000) 11110.
[35] F. Fally, V. Perrichon, H. Vidal, Catal. Today 59 (2000) 373.
[36] X.D. Wu, J. Fan, R. Rui, Chem. Eng. J. 109 (2005) 133.
[37] C. Bozo, N. Guilhaume, J.-M. Herrmann, J. Catal. 203 (2001) 393.
[38] M. Boaro, A. Trovarelli, J.H. Hwang, Solid State Ionics 147 (2002) 85.